EFFECTS OF PENETRATIVE CONVECTION ON SOLAR DYNAMO

Youhei Masada[1], Kohei Yamada[1] and Akira Kageyama [1]
Submitted to ApJ Letters, Preprint typeset using LATEXstyle

ABSTRACT

Spherical solar dynamo simulations are performed. Self-consistent, fully compressible magnetohydrodynamic system with a stably stratified layer below the convection zone are numerically solved with a newly developed simulation code based on the Yin-Yang grid. The effects of penetrative convection are studied by comparing two models with and without the stable layer. A solar-like differential rotation profile is established when the penetrative convection is taken into account without assuming any forcing. A large-scale magnetic field is also spontaneously organized in the underlying stable layer. The embedded field has a dipole symmetry about the equator and it shows polarity reversals in time.
Subject headings: convection–magnetohydrodynamics (MHD) – Sun: dynamo – Sun: interior

1. INTRODUCTION

Solar interior is a frontier of the solar physics. A grand challenge is a construction of self-consistent theory that explains the observed large-scale spatial structures of the fields and their dynamical change in time with the pseudo-periodicity of 22 years. Two basic large-scale structures that should be explained are the azimuthal average of the azimuthal flow, $\bar{v}_\phi$, and the azimuthal average of the azimuthal magnetic field, $\bar{B}_\phi$. See Ossendrijver 2003; Miesch 2012 for reviews of the solar interior.

To reproduce the large-scale structures and dynamics, magnetohydrodynamics (MHD) simulations have been performed both in the global (spherical shell) geometry (e.g., Gilman 1983; Glatzmaier 1985; Brun et al. 2004) and in the local Cartesian geometry (e.g., Nordlund et al. 1992; Brandenburg et al. 1996; Cattaneo et al. 2003). The exponential growth of the computer performance has yielded breakthroughs to the solar dynamo simulation research. Browning et al. (2006) showed in spherical shell dynamo simulations that strong axisymmetric toroidal magnetic fields can be formed in stably stratified layer below the convection zone. A latitudinal thermal forcing was, however, necessary for keeping the solar-like differential rotation profile in their simulation. Brun et al. (2011) performed hydrodynamic simulations, without magnetic fields, in which the solar-like convection profile with a tachocline can be formed without any forcing. An anelastic model was adopted in these two simulations.

Ghizaru et al. (2010) and Racine et al. (2011) showed that the large-scale magnetic field in the stable layer exhibits polarity reversals when the temporal integration of the simulation is calculated for long enough. Their simulation is also based on an anelastic model that is popularly used in the global circulation models of the earth's atmosphere with a cooling term to force the system toward the ambient state.

In this Letter, we report the first fully compressible spherical solar dynamo simulation with a stably stratified layer below the convection zone. Formations of the key profile of the solar interior, i.e., the solar-like $\bar{v}_\phi$ &

$\bar{B}_\phi$, and the spontaneous polarity reversals are simulated, without assuming any forcing in the fundamental equations. To elucidate the effects of the penetrative convection, two simulations with and without the stable layer below the convection zone are compared.

Another purpose of this Letter is to report a development of new program code for the solar dynamo simulation. Most simulation models of the global solar dynamo are spectral-based type, using the spherical harmonics expansion (e.g., Brun et al. 2004). The spherical harmonics expansion method is, however, believed to be confronted with the parallel scaling difficulty when tens of thousands, or more, processor cores are used. A different approach to massively parallel solar dynamo model is strongly required for the present peta- or coming exascale era. We have developed a global solar dynamo simulation code based on the grid point-based approach.

The spherical geometry imposes difficulties in the design of the spatial grid points to sustain high numerical efficiency, accuracy, and parallel scalability. We have proposed an overset grid method approach to the spherical geometry (Kageyama & Sato 2004). The grid system, Yin-Yang grid, is applied to geodynamo (e.g., Kageyama et al. 2008; Miyagoshi et al. 2010), mantle convection (e.g., Kameyama et al. 2008; Tackley 2008), supernova explosions (e.g., Müller et al. 2012; Lentz et al. 2012), and other astro- and geophysical simulations. The parallel scaling property of the spherical MHD simulation on the Yin-Yang grid is promising. It attained 46% (15.2 TFlops) of the peak performance of 4096 cores of the Earth Simulator supercomputer for the geodynamo simulations (Gordon Bell Award in Supercomputing 2004). Our new solar dynamo code is developed based on this Yin-Yang geodynamo code. This Letter is our first report on the results obtained by this Yin-Yang solar dynamo code.

2. NUMERICAL SETTINGS

We numerically solve an MHD dynamo convection system in a spherical shell domain defined by ($0.6R \leq r \leq R$), ($0 \leq \theta \leq \pi$), and ($-\pi \leq \phi \leq \pi$), where r, θ, and ϕ are radius, colatitude, and longitude, respectively. Our model has two layers: upper convective layer of thickness $0.3R$ in the range of ($0.7R \leq r \leq R$), and stably stratified lower layer of thickness $0.1R$ in ($0.6R \leq r \leq 0.7R$).

[1] Department of Computational Science, Graduate School of System Informatics, Kobe University; Kobe, Japan, contact: ymasada@harbor.kobe-u.ac.jp
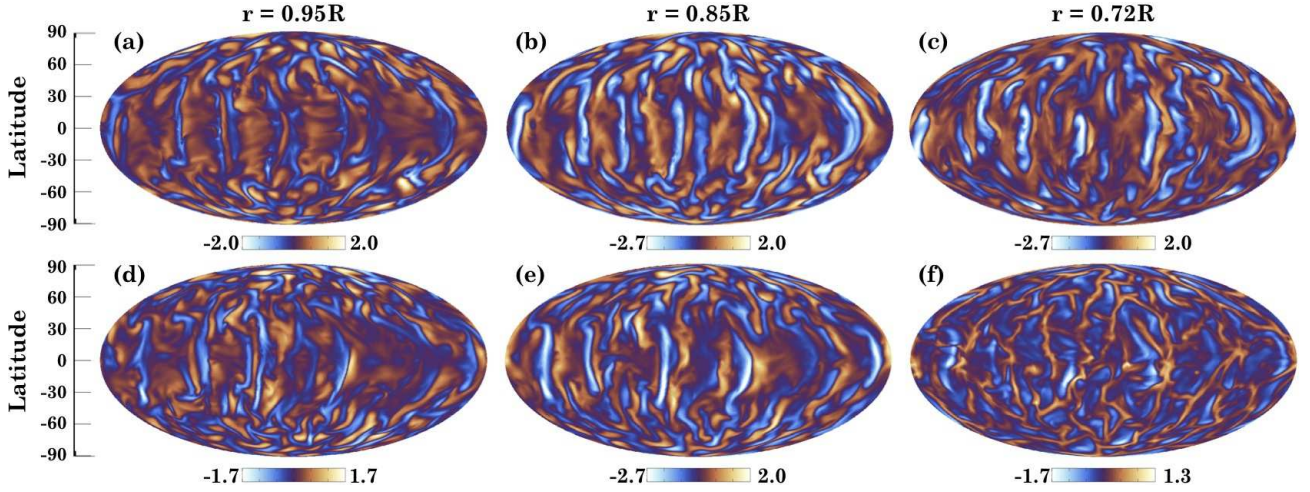
FIG. 1.— The radial velocity profile $v_r(r, \theta)$ when $t = 330\tau_c$, in the Mollweide projection, on spherical surfaces at different depths for two models A and B. The panels (a)–(c) correspond to the depths $r = 0.95R$, $0.85R$ and $0.72R$ for Model A, and the panels (d)–(f) are those for Model B. The orange and blue tones depict upflow and downflow velocities.

The fundamental equations are the fully compressible MHD equations in the rotating frame of reference with a constant angular velocity $\mathbf{\Omega}$ which is parallel to the coordinate axis ($\theta = 0$):

$$\frac{\partial \rho}{\partial t} = -\nabla \cdot \boldsymbol{f} \,, \tag{1}$$

$$\frac{\partial \boldsymbol{f}}{\partial t} = -\nabla \cdot (\boldsymbol{v}\boldsymbol{f}) - \nabla p + \boldsymbol{j} \times \boldsymbol{B} + \rho \boldsymbol{g} + 2\rho \boldsymbol{v} \times \boldsymbol{\Omega} + \boldsymbol{Q} \,, \tag{2}$$

$$\frac{\partial p}{\partial t} = -\boldsymbol{v} \cdot \nabla p - \gamma p \nabla \cdot \boldsymbol{v} + (\gamma - 1)\Phi \,, \tag{3}$$

$$\frac{\partial \boldsymbol{A}}{\partial t} = \boldsymbol{v} \times \boldsymbol{B} - \eta \boldsymbol{j} \,, \tag{4}$$

with $\boldsymbol{g} = -g_0/r^2 \boldsymbol{e}_r$, $\boldsymbol{B} = \nabla \times \boldsymbol{A}$, $\boldsymbol{j} = \nabla \times \boldsymbol{B}$, and $\Phi = \nabla \cdot (\kappa \nabla T) + 2\nu \boldsymbol{S}^2 + \eta \boldsymbol{j}^2$. The mass density ρ, pressure p, mass flux density $\boldsymbol{f} = \rho \boldsymbol{v}$, magnetic field's vector potential $\boldsymbol{A}$ are the basic variables. We assume an ideal gas law $p = (\gamma-1)\rho\epsilon$ with $\gamma = 5/3$, where ϵ is the internal energy. The viscosity, magnetic diffusivity, and thermal conductivity are represented by ν, η, and κ respectively. The viscous term $\boldsymbol{Q}$ is written by $Q_i = \partial_j (2\nu S_{ij})$ with the strain tensor

$$S_{ij} = \frac{1}{2} \left(\frac{\partial v_i}{\partial x_j} + \frac{\partial v_j}{\partial x_i} - \frac{2}{3}\delta_{ij}\nabla \cdot \boldsymbol{v} \right) \,. \tag{5}$$

In the program code, the tensor components are written in the spherical polar coordinate.

The initial condition is a hydrostatic equilibrium which is described by a piecewise polytropic distribution with the polytropic index m,

$$\frac{dT}{dr} = \frac{g}{c_v(\gamma - 1)(m + 1)} \,, \tag{6}$$

(e.g., Käpylä et al. 2010). We choose $m = 1$ and 3 for the upper convection layer and the lower stable layer, respectively. The thermal conductivity is determined by requiring a constant luminosity L, defined by $L \equiv -4\pi\kappa r^2 \partial T/\partial r$, throughout the domain.

Non-dimensional quantities are defined by setting $R = g_0 = \rho_0 = 1$ where ρ_0 is the initial density at $r = 0.6R$. We normalize length, time, velocity, density, and magnetic field in units of R, $\sqrt{R^3/g_0}$, $\sqrt{g_0/R}$, ρ_0 and $\sqrt{g_0\rho_0/R}$. We define the Prandtl, magnetic Prandtl, and Rayleigh numbers by

$$\mathrm{Pr} = \frac{\nu}{\bar{\chi}}, \quad \mathrm{Pm} = \frac{\nu}{\eta}, \quad \mathrm{Ra} = \frac{GMd^4}{\nu\bar{\chi}R^2} \left(-\frac{1}{c_p}\frac{\mathrm{d}s}{\mathrm{d}r} \right)_{r_m} \,, \tag{7}$$

where $\bar{\chi} \equiv \kappa_m/(c_p\rho_m)$ is the thermal diffusivity at the mid-convection zone ($r = r_m$), and $d = 0.3R$ is the depth of the convection zone. The stratification level is controlled by the normalized pressure scale height at the surface, $\xi_0 \equiv c_v(\gamma-1)T_s/(g_0/R)$, where T_s is the temperature at $r = R$. In this work, we use $\xi_0 = 0.3$, yielding a small density contrast about 3.

The relative importance of rotation in the convection is measured by the Coriolis number defined by $\mathrm{Co} = 2\Omega_0 d/v_{\mathrm{rms}}$, where $v_{\mathrm{rms}} \equiv [\langle v_\theta^2 + v_r^2 \rangle]^{1/2}$ is the mean velocity. The angular brackets denote the time and volume average in the upper convective layer at the saturated state. The convective turn-over time and the equipartition strength of magnetic field are defined by $\tau_c \equiv d/v_{\mathrm{rms}}$ and $B_{\mathrm{eq}} \equiv \langle \rho (v_\theta^2 + v_r^2) \rangle^{1/2}$.

The stress-free boundary condition for the velocity is imposed on the two spherical boundaries. We assume the perfect conductor boundary condition for the magnetic field ($A_r = A_\theta = A_\phi = 0$) on the inner surface, and the radial field condition ($A_r = 0, \partial A_\theta/\partial r = -A_\theta/r, \partial A_\phi/\partial r = -A_\phi/r$) on the outer surface. A constant energy flux is imposed on the inner boundary. The temperature is fixed to be T_s on the outer boundary.

The eqs. (1)–(4) are discretized by the second-order central difference on the Yin-Yang grid. Each of the two congruent grids, Yin-grid and Yang grid, covers a partial spherical shell region defined as ($\pi/4 \leq \theta \leq 3\pi/4, -3\pi/4 \leq \phi \leq 3\pi/4$). They are combined in a complemental way to cover a whole spherical shell. Physical quantities on the horizontal boarders of Yin- or Yang-grid are set by mutual interpolations. For the time integration, the standard fourth-order Runge-Kutta method is used. Since the Yin-Yang grid is free from the coordinate singularity and the grid concentration around there, we can avoid the severe time-step constraint due to the CFL condition. See Kageyama & Sato 2004 for more detail on the Yin-Yang grid method. The computation is

performed in parallel using MPI (Message Passing Interface).

Non-dimensional parameters Pr = 0.2, Pm = 4.0, and Ra = 1.2×10^5, and constant angular velocity of $\Omega_0 = 0.4$ are adopted in all the calculations reported here. The total grid size for the run with the upper convection layer and the lower stable layer (Model A) is 121 (in r) $\times 402$ (in θ) $\times$ 402 (in ϕ) $\times 2$ (Yin & Yang). A model without the stable layer (Model B) is also studied, in the domain $(0.7R \leq r \leq R)$, with the same physical parameters and the same grid spacings ($91 \times 402 \times 402 \times 2$). A random temperature perturbation and weak magnetic field are seeded in the convection zone when the calculation starts.

3. NUMERICAL RESULTS

3.1. *Convection and Mean Flows*

After the convective motion sets in, it reaches a nonlinear saturation state at around $t = 10\tau_c$. The saturation levels of the convection kinetic energy for Model A and B are almost the same. The mean velocity is $v_{\rm rms} = 0.03$ which yields $B_{\rm eq} = 0.02$, Co = 8.0 and $\tau_c = 10.0$ for both models. We have run the simulations till $500\tau_c$ and then compare physical properties of convections, mean flows and magnetic dynamos between two models. The flow velocity and magnetic flux density are normalized by $v_{\rm rms}$ and $B_{\rm eq}$ respectively in the following.

Figure 1 shows, in the Mollweide projection, the radial velocity profile v_r when $t = 330\tau_c$ on spherical surfaces at different depths for two models. The panels (a)–(c) correspond to the depths $r = 0.95R$, $0.85R$ and $0.72R$ for Model A, and the panels (d)–(f) are those for Model B. The orange and blue tones depict upflow and downflow velocities. At the upper ($r = 0.95R$) and mid ($r = 0.85R$) convection zones, the convective motion is characterized by upflow dominant cells surrounded by networks of narrow downflow lanes for both models. The higher the latitude, the smaller the convective cell prevails. Elongated columnar convective cells aligned with the rotation axis appear near the equator. These are the typical features observed in rotating stratified convection (e.g., Spruit et al. 1990; Miesch et al. 2000; Brummell et al. 2002). In panel (c), we find that the downflow lanes persist the plume-like coherent structure even just above the bottom of the unstable layer ($r = 0.72R$). The downflow plumes then penetrate into the underlying stable layer. As a result, mean zonal and meridional flows are driven by the Reynolds stress in the stable layer.

In Figures 2(a) and (b), time-averaged mean angular velocity, defined by $\bar{\Omega}(r, \theta) = \bar{v}_\phi/(r \sin \theta) + \Omega_0$, is shown for the models A and B, respectively. Here the overbar denotes the time and azimuthal average. The time average spans in the range of $300\tau_c \leq t \leq 400\tau_c$. While the overall structures –especially the equatorial acceleration– are common in the two models A and B, some differences between them are noticeable. Model B exhibits a cylindrical rotation profile which has iso-rotation contours aligned with the rotation axis. The system is dominated by the Taylor-Proudman balance in this case (Pedlosky 1987). In contrast to that, a differential rotation with conical iso-rotation surfaces at mid-latitude is established in Model A. More importantly, a strong radial gradient of the angular velocity is developed in the stably stratified layer around latitudes ±40°. This structure is reminis-

cent of the solar tachocline despite the radial shear layer is broad compared to the observed one (Hughes et al. 2007). The rotation profile of Model A is reasonably similar with that of the Sun deduced from helioseismology (Thompson et al. 2003). This confirms that the stable layer underlying the convective envelope has a role in maintaining the solar-like differential rotation as reported in the hydrodynamic model of Brun et al. (2011).

Shown in Figures 2(c) and (d) are time-averaged mean meridional flows for the models A and B. The color contour depicts the absolute value of the meridional flow velocity with a maximum $\sim 0.1v_{\rm rms}$. Overplotted are streaklines with a length proportional to the flow speed. The circulation flow is primarily counter-clockwise in the bulk of the convection zone in the northern hemisphere, that is, the poleward in the upper convection zone and the equatorward in the bottom convection zone in both models. There is however a clear difference in the circulation pattern between the two models. While a large single-cell is formed in Model B, Model A shows a double-cell pattern with a strong inward/outward flow at the low/mid latitudes as suggested by the helioseismic inversion (see Mitra-Kraev & Thompson 2007). An intriguing finding is that the equatorward component penetrates into the underlying stable layer when the strong radial gradient of the angular velocity resides. The penetrative transport of magnetic flux by the meridional flow might play a role in magnetic dynamo in our model.

3.2. *Structure and Evolution of Magnetic Fields*

The magnetic energy is amplified by the dynamo action and is saturated at a level of about 40% of the convective kinetic energy for both models after $t \simeq 20\tau_c$. A snapshot of the azimuthal component of the magnetic field B_ϕ at $t = 330\tau_c$ is presented in Figure 3 on a spherical surface at the depths (a) $r = 0.62R$ and (b) $r = 0.85R$ for Model A, and (c) $r = 0.85R$ for Model B. The orange and blue tones depict positive and negative values of the B_ϕ component. The magnetic field lines at the time and position corresponding to those in the panels (a)–(c) are visualized in Figures 3(d)–(f), respectively.

The convective envelope is dominated by disordered tangled magnetic field lines with a myriad of localized small-scale structures in both models. These incoherent magnetic fields are strongly influenced by vigorous convective motions and thus are highly intermittent. The horizontal converging flows sweep magnetic fields into downflow lanes and intensify them locally to the super-equipartition strength as was observed in convective dynamo simulations (e.g., Brandenburg et al. 1996; Cattaneo et al. 2003; Brun et al. 2004).

In the underlying stable layer of Model A, a strong large-scale azimuthal component is built up and stored for long time intervals. This well-organized magnetic component is roughly antisymmetric about the equatorial plane and reaches a maximum strength of $2B_{\rm eq}$. The large-scale component grows in the region where the strong radial shear resides (see Figure 2(a)). This would be an important evidence of a connection between the deep-seated coherent fields and the strong radial shear layer. These results suggest that the stably stratified layer is a key component to organize large-scale magnetic fields and support numerical studies of Browning et al. (2006) and Ghizaru et al. (2010).
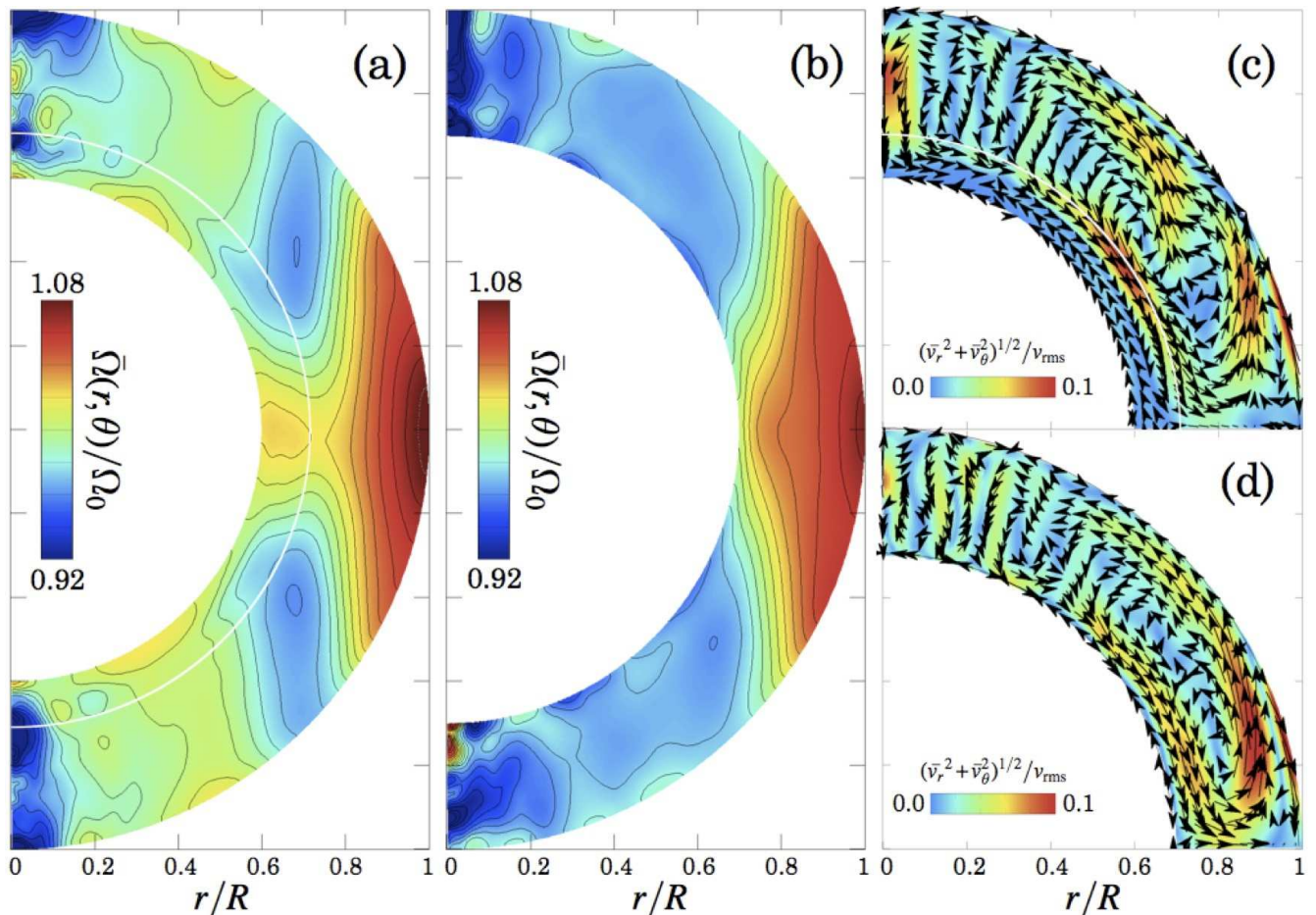
FIG. 2.— Time-averaged mean angular velocity $\bar{\Omega}(r,\theta)$ [panels (a) and (b) for Models A and B], and mean meridional flow [panels (c) and (d) for Models A and B], where $\bar{\Omega}(r,\theta) \equiv \bar{v}_\phi/(r\sin\theta) + \Omega_0$. The white solid curves in panel(a) and (c) denote the interface between the convection and stable layers.

One of the most interesting findings in our simulation is that the deep-seated magnetic fields in the stable layer show polarity reversals. Figure 4 gives an azimuthally-averaged magnetic field as a function of time and latitude. The panels (a), (b) and (c) represent $\bar{B}_r$, $\bar{B}_\theta$, and $\bar{B}_\phi$ at $r = 0.65R$ for Model A. The large-scale $\bar{B}_\phi$ with antisymmetric parity persists over a relatively long period despite strong stochastic disturbances due to penetrative convective motions. The $\bar{B}_\phi$ component changes the sign for at lest three times, at about $t = 100\tau_c$, $t = 200\tau_c$, and $t = 350\tau_c$ [panel (c)].

As for the poloidal component of the magnetic field, it shows the dipole dominance. During 30–$100\tau_c$ when strong $\bar{B}_\phi$ component with positive polarity dominates in the northern hemisphere, negative $\bar{B}_r$ and positive $\bar{B}_\theta$ are observed [panels (a) and (b)]. While the $\bar{B}_\theta$ component has the same sign in both the hemispheres, the $\bar{B}_r$ component has opposite polarity in the two hemispheres. When the $\bar{B}_\phi$ reversal takes place, the other two components $\bar{B}_r$ and $\bar{B}_\theta$ also change the sign. See, for example, at about $t = 100\tau_c$ in Fig. 4.

The overall features indicate that the large-scale magnetic field has a dipole-like component rooted in the stably stratified layer and reverses its dipole polarity, accompanied by the polarity reversal of the $\bar{B}_\phi$ component as shown in Figure 5 schematically.

4. SUMMARY

We reported, in this Letter, our first results of solar dynamo simulation based on the Yin-Yang grid with the fully compressible MHD model. To investigate influences of the stably stratified layer below the convection zone, two simulation models with and without the stable layer were compared.

It is confirmed that the stable layer has substantial influence on the convection and the magnetic field. The differential rotation profile inferred from the helioseismology is simulated when the stable layer is taken into account. The conical iso-rotation surfaces at the mid latitudes is established in the convective envelope. The strong radial shear layer, which is reminiscent of the solar tachocline, is formed just beneath the convection zone as a result of the penetrative convection.

The stably stratified layer would be a key component not only for maintaining the solar-like differential rotation but also for organizing large-scale magnetic fields. In our model, the strong large-scale azimuthal component with antisymmetric parity about the equator is built up in the underlying stable layer, whereas the convective envelope is dominated by highly intermittent disordered magnetic fields. An intriguing finding is that the large-scale magnetic fields embedded in the stable layer undergo polarity reversals. Although a full description of
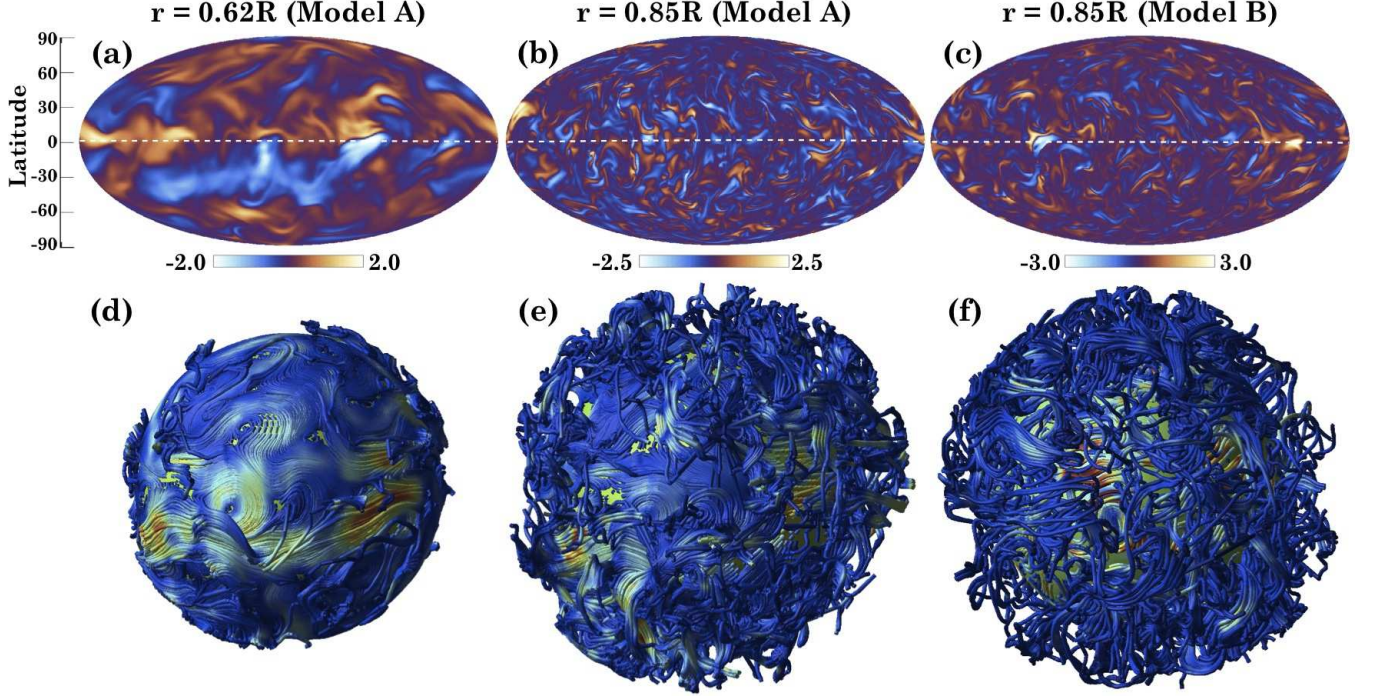
FIG. 3.— A snapshot of the azimuthal component of the magnetic field B_ϕ when $t = 330\tau_c$ on a spherical surface at the depths (a) $r = 0.62R$ and (b) $r = 0.85R$ for Model A, and (c) $r = 0.85R$ for Model B. The orange and blue tones depict positive and negative values of the B_ϕ component. The magnetic field lines at the time and position corresponding to those in the panels (a)–(c) are visualized in the panels (d)–(f), respectively
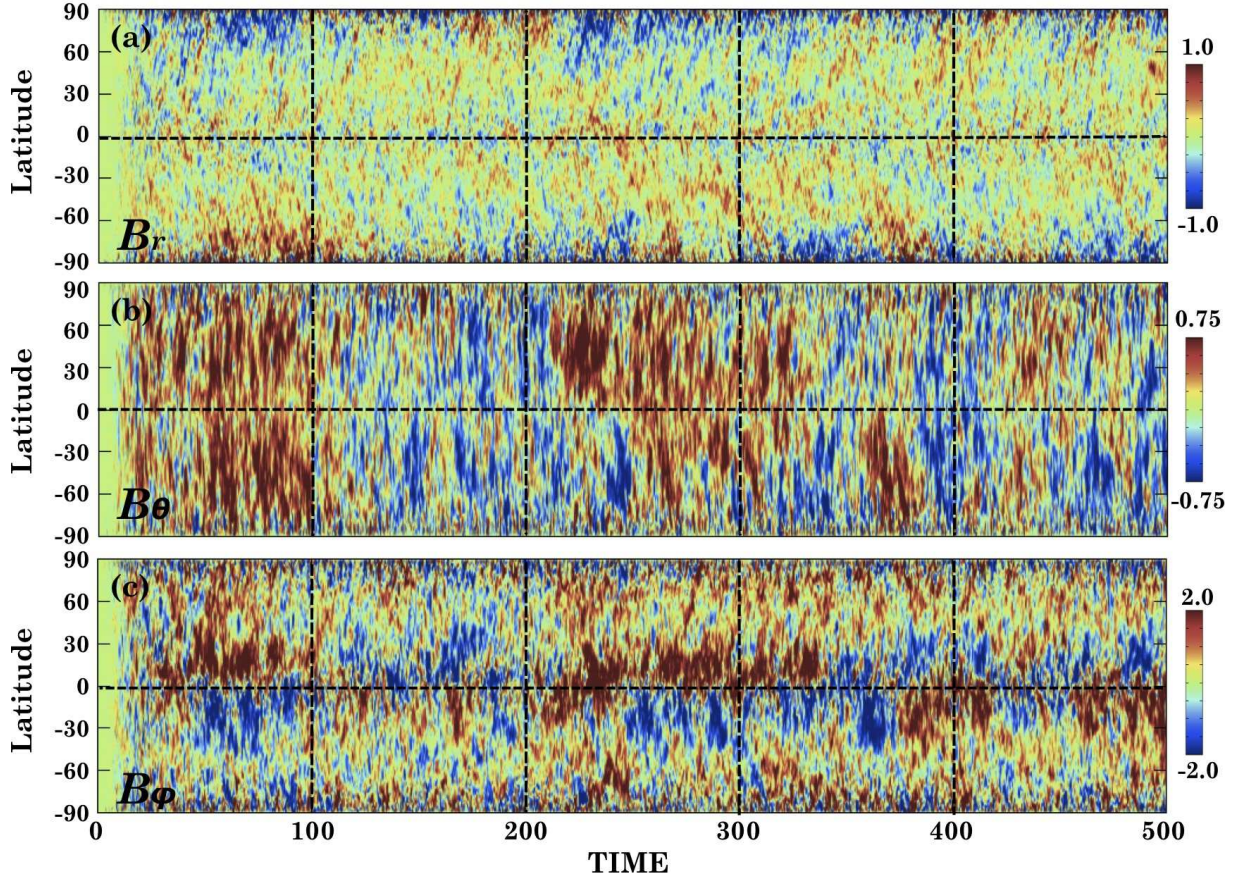

FIG. 4.— An azimuthally-averaged magnetic field as a function of time and latitude. The top, middle and bottom panels correspond to $\bar{B}_r$, $\bar{B}_\theta$, and $\bar{B}_\phi$ at the depths $r = 0.65R$ in Model A. The red and blue tones depict positive and negative values of each component.

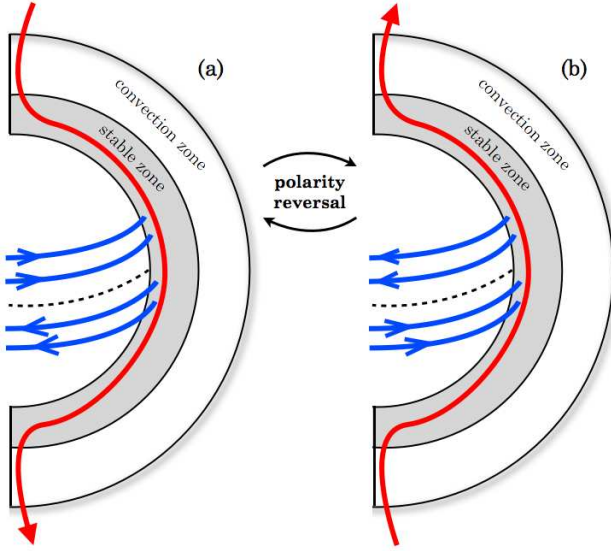developed just beneath the convection zone is closely related to the dynamo process.

All the dynamo simulations reported here have used a relatively weak stratification with the density contrast of about 3 (see §2). The strong stratification in the real Sun may influence on the physical properties of convections, mean flows and magnetic dynamo (Käpylä et al. 2013). It would be interesting that the three key features, solar-like $\bar{v}_\phi$, $\bar{B}_\phi$, and the polarity reversals are self-consistently reproduced, without assuming any forcing, even in the modest density stratification. Higher resolution simulations with a more realistic density stratification will facilitate our understanding of the physics of the solar convection and the solar dynamo, that is our next step with the Yin-Yang solar dynamo simulation code.

Fig. 5.— Schematic picture of the large-scale magnetic field deep-seated in the convectively stable layer. The blue and red curves demonstrate the azimuthal and poloidal magnetic components. The large-scale magnetic field has a dipole-like component and reverses its dipole polarity, accompanied by the polarity reversal of the $\bar{B}_\phi$ component.

the dynamo mechanism is beyond the scope of this Letter, here we mention that the strong radial shear layer

REFERENCES

Brandenburg, A., Jennings, R. L., Nordlund, Å., et al. 1996, Journal of Fluid Mechanics, 306, 325

Browning, M. K., Miesch, M. S., Brun, A. S., & Toomre, J. 2006, ApJ, 648, L157

Brummell, N. H., Clune, T. L., & Toomre, J. 2002, ApJ, 570, 825

Brun, A. S., Miesch, M. S., & Toomre, J. 2004, ApJ, 614, 1073

Brun, A. S., Miesch, M. S., & Toomre, J. 2011, ApJ, 742, 79

Cattaneo, F., Emonet, T., & Weiss, N. 2003, ApJ, 588, 1183

Glatzmaier, G. A. 1985, ApJ, 291, 300

Gilman, P. A. 1983, ApJS, 53, 243

Ghizaru, M., Charbonneau, P., & Smolarkiewicz, P. K. 2010, ApJ, 715, L133

Hughes, D. W., Rosner, R., & Weiss, N. O. 2007, The Solar Tachocline,

Kageyama, A., & Sato, T. 2004, Geochemistry, Geophysics, Geosystems, 5, 9005

Kageyama, A., Miyagoshi, T., & Sato, T. 2008, Nature, 454, 1106

Kameyama, M., Kageyama, A., & Sato, T. 2008, Physics of the Earth and Planetary Interiors, 171, 19

Käpylä, P. J., Korpi, M. J., Brandenburg, A., Mitra, D., & Tavakol, R. 2010, Astronomische Nachrichten, 331, 73

Käpylä, P. J., Mantere, M. J., & Brandenburg, A. 2012, ApJ, 755, L22

Käpylä, P. J., Mantere, M. J., Cole, E., Warnecke, J., & Brandenburg, A. 2013, arXiv:1301.2595

Lentz, E. J., Bruenn, S. W., Harris, J. A., et al. 2012, Proc. 12th Symposium on Nuclei in the Cosmos. PoS(NIC XII) 208

Miesch, M. S., Elliott, J. R., Toomre, J., Clune, T. L., Glatzmaier, G. A., & Gilman, P. A. 2000, ApJ, 532, 593

Miesch, M. S. 2012, Royal Society of London Philosophical Transactions Series A, 370, 3049

Mitra-Kraev, U., & Thompson, M. J. 2007, Astronomische Nachrichten, 328, 1009

Miyagoshi, T., Kageyama, A., & Sato, T. 2010, Nature, 463, 793

Müller, E., Janka, H.-T., & Wongwathanarat, A. 2012, A&A, 537, A63

Nordlund, A., Brandenburg, A., Jennings, R. L., et al. 1992, ApJ, 392, 647

Ossendrijver, M. 2003, A&A Rev., 11, 287

Pedlosky, J. 1987, Geophysical Fluid Dynamics, by Joseph Pedlosky. Springer, New York. 1987

Racine, É., Charbonneau, P., Ghizaru, M., Bouchat, A., & Smolarkiewicz, P. K. 2011, ApJ, 735, 46

Spruit, H. C., Nordlund, A., & Title, A. M. 1990, ARA&A, 28, 263

Tackley, P. J. 2008, Physics of the Earth and Planetary Interiors, 171, 7

Thompson, M. J., Christensen-Dalsgaard, J., Miesch, M. S., & Toomre, J. 2003, ARA&A, 41, 599

Tobias, S. M., Brummell, N. H., Clune, T. L., & Toomre, J. 2001, ApJ, 549, 1183